

Tempering Effects of Multitrack Laser Surface Heat Treatment of AISI 1045 Steel

Chi-Liang Kung,¹ Hao-En Shih,² Chao-Ming Hsu,^{1*} and Cheng-Yi Chen^{3,4**}

¹Department of Mechanical Engineering, National Kaohsiung University of Science and Technology, Kaohsiung 80778, Taiwan

²Department of Mechanical and Electro-Mechanical Engineering, National Sun Yat-sen University, Kaohsiung 804, Taiwan

³Department of Electrical Engineering, Cheng Shiu University, Kaohsiung 83347, Taiwan

⁴Super Micro Mass Research and Technology Center, Cheng Shiu University, Kaohsiung 83347, Taiwan

(Received November 30, 2018; accepted January 11, 2019)

Keywords: laser surface heat treatment, hardening width, hardening depth, tempering effect

A thermo-elastic-plastic finite element model was employed to simulate and analyze the effects of high-power parameters on the laser heat treatment of AISI 1045 steel. Tempering effects of multitrack laser heat treatment using various process parameters—laser power, laser feed rate, laser overlap rate, and laser spot size—were analyzed to estimate the distribution of a hardening layer on the steel surface. Numerical simulation results indicated that the proposed finite element model is effective in analyzing the laser heat treatment of the steel surface and calculating the possibility of decreases in steel hardness due to tempering effects, enabling it to undergo rapid temperature increases and decreases.

1. Introduction

Laser surface processing technology has undergone more than 40 years of development and has been applied by numerous well-known international enterprises in the automotive, aerospace, military, shipbuilding, and material-related industries because of its abundant advantages for manufacturing the products of these industries. Unlike the conventional heat treatment method, laser surface heat treatment involves transmitting a laser beam through optics to irradiate a high-energy, high-intensity laser beam onto a metal surface to immediately facilitate austenite transformation. At room temperature and without any fixed thermal convection conditions, the austenite form of the metal surface undergoes martensitic transformation through self-quenching.⁽¹⁾

In 1960, Maiman^(2,3) installed a ruby cylinder (diameter: 1 cm; length: 2 cm) on the axis of a helical xenon flashlamp, which was then inserted into a polished aluminum cylinder. When the ruby cylinder was illuminated by the flashlamp, the device emitted red light; hence, the first working laser was invented. According to DeMichelis,⁽⁴⁾ a German scientist used a laser beam to perform heat treatment on a metal, which was the first experiment in history

*Corresponding author: e-mail: jammy@kuas.edu.tw

**Corresponding author: e-mail: k0464@gcloud.csu.edu.tw

<https://doi.org/10.18494/SAM.2019.2229>

to employ lasers as a heat treatment method. Scientists in the United States then started to study the absorption and hardening of a graphite-coated metal surface irradiated with a ruby laser beam.⁽⁵⁾ Researchers in the United States and Japan^(6,7) also began to examine the heat treatment ability of lasers on metal surfaces by observing their austenitization and to study the effects of laser heat treatment on alloys. In 1965, the Nd:YAG laser was the first industrial use of this technology to repair connectors inside assembled television tubes.⁽⁸⁾ Lasers were applied to industrial production in 1974, when the Saginaw Steering Gear Division, part of General Motors, began to use laser beams to harden steering gear housings.^(9,10) Loeffler⁽¹¹⁾ proposed the first computer numerical control (CNC) laser soldering machine, which used a CO₂ laser and keyhole welding technology. However, no mature dynamic equations were developed in related research until 1995, when Fuerschbach and MacCallum⁽¹²⁾ irradiated a CO₂ laser beam onto 304 stainless steel at 6 MW/cm² and derived the relationship among laser absorption rate, weld pool width, and weld pool depth using a weld pool geometry model.

Laser surface heat treatment has the following advantages:⁽¹⁾ First, it causes the metal to self-quench; thus, the metal surface remains clean and does not require further cleaning after treatment. Second, changing the laser power and the position of the optics enables its application in heat treatment processes for different materials with different requirements. Third, laser sources installed on CNC machines can be used to perform heat treatment on workpieces with complex shapes. Fourth, workpieces that have received laser heat treatment undergo minimal deformation. Fifth, workpieces that have received laser heat treatment do not require grinding. Sixth, production can be automated, effectively reducing human resource costs.

Bojinović *et al.*⁽¹³⁾ proposed a 3D model of the laser hardening process using a high-power diode laser for 50CrV4 steel, based on the finite element method. Nguyen and Yang⁽¹⁴⁾ presented a sequential method to estimate surface absorptivity in the laser surface hardening process using a 1D transient conduction heat transfer model. Sarkar *et al.*⁽¹⁵⁾ proposed a modified 1D heat conduction model to analyze the effects of temperature and surface hardening on low-carbon thin steel (thickness: 1 mm) using an Yb-fiber laser. Martínez *et al.*⁽¹⁶⁾ proposed a scanner-based laser hardening process for AII045 steel and discussed the effects of scanning speed on the hardened layer thickness. Lakhkar *et al.*⁽¹⁷⁾ proposed a numerical model to predict the back tempering in multitrack laser hardening for AISI4140 steel. Recently, Cordovilla *et al.*⁽¹⁸⁾ have studied laser surface hardening analysis to propose the design of a suitable overlapping distance for Cr-Mo steel. Overall, the main difficulties are how to choose adequate laser technological parameters and a suitable laser scanning (tracking) method for surface hardening to obtain the optimum hardening quality with an excellent temperature field distribution.

In this study, the temperature distribution of SAE-AISI 1045, a medium carbon steel, was analyzed by adopting the finite element method as the numerical simulation tool and employing a neodymium-doped yttrium aluminum garnet (Nd:YAG) solid-state laser as the laser source.⁽¹⁹⁾ The material properties of SAE-AISI 1045 were obtained from Ding and Yung.⁽²⁰⁾ In addition, on the basis of studies by Kusuhara *et al.*,⁽²¹⁾ a thermo-elastic-plastic finite element model was constructed to examine and discuss the effects of laser feed rate, laser power, and laser spot

size on the temperature distribution, the depth of the hardened layer (hardening depth), and the width of the laser-hardened area (hardening width). Moreover, the effects of the overlap and power level of a diode laser beam on the hardened layer depth of SAE-AISI 1045 were examined.

2. Finite Element Modeling and Analysis

By simulating and analyzing the application of a moving Gaussian laser beam as the source for the heat treatment of a tool steel surface, a set of research procedures to identify the adequate ranges of various process parameters was established in this study. We used a multitrack laser beam with a Gaussian profile to perform heat treatment under the effects of circular laser spots and examined the possible tempering effects of the laser beam during the heat treatment process. The details are described below.

2.1. Setup of moving heat source

The employed Nd:YAG laser was adjusted for heat source distribution in transverse electromagnetic mode 00 (TEM₀₀), as described in Ref. 22. This commonly used mode differs from that of a conventional welding heat source, which exhibits a bi-elliptic distribution. In the TEM₀₀ mode, the power density is highest at the center of the beam and diminishes with increasing distance from the center, resulting in a Gaussian distribution of light intensity across the beam diameter. The power density of the laser (E_e) in the TEM₀₀ mode can be expressed as

$$E_e(r_e) = P_i \cdot \Phi(r_e), \quad (1)$$

where r_e is the distance from the center of a laser beam, P_i is the laser power size, and F is the Gaussian distribution function. The center of the 2D Gaussian distribution was rotated 360° to obtain a 3D Gaussian distribution, which is expressed as

$$\Phi(r_e) = \frac{1}{2\pi s^2} \exp\left(-\frac{r_e^2}{2s^2}\right), \quad (2)$$

where s is the standard deviation of the Gaussian distribution. In accordance with the research in Refs. 22 and 24, the radius of the spot size, R_e , was used to calculate the area in which 95% of the laser beam power passes through a circle of its focused area, which can be written as

$$\int_0^{2\pi} \int_0^{R_e} \frac{1}{2\pi s^2} e^{-\frac{r_e^2}{2s^2}} r_e dr_e d\theta = 0.95, \quad (3)$$

where θ is the angular variable. From Eq. (3), the following can be obtained:

$$s = \frac{R_e}{\sqrt{2 \ln(20)}} \approx \frac{R_e}{\sqrt{6}}. \quad (4)$$

Substituting Eq. (4) to Eq. (2), Eq. (1) can be rewritten as

$$E_e(r_e) = \frac{3P_i}{\pi R_e^2} \exp\left(-\frac{3r_e^2}{R_e^2}\right). \quad (5)$$

Because most materials are unable to fully absorb the energy of a laser beam, we considered the effects of the steel thermal absorptivity (η_e). Referring to the data presented by DeKock,⁽²⁵⁾ we set the thermal absorption rate h_e at 40%; thus, the final amount of energy absorbed by the steel (P_e) can be expressed as

$$P_e = \eta_e \cdot \frac{3P_i}{\pi R_e^2} \exp\left(-\frac{3r_e^2}{R_e^2}\right). \quad (6)$$

The diameter of the laser spot set between 2 and 4 mm is chosen in this study.

2.2. Construction of finite element model

In this study, MSC.MARC, a commercial finite element analysis software program, was used as a numerical equation solving tool, and the pre- and post-Mentat processor provided by MSC.MARC was employed to construct a finite element model mesh and boundary conditions, and to obtain the temperature and stress data for the analysis node. AISI 1045 medium carbon steel was selected in bar-shaped pieces with dimensions of $100 \times 12 \times 6 \text{ mm}^3$ ($l \times w \times h$). The use of a 3D finite element model mesh for multitrack laser heat treatment was proposed, as shown in Fig. 1. Note that the mesh in the x - and y -directions is evenly distributed, but the mesh in the z -direction is smaller when close to the material surface. The moving heat source of the laser with heat distribution in the TEM₀₀ Gaussian mode was simulated using MSC.MARC, as shown in Fig. 2.

2.3. Multitrack laser heat treatment model

Steel materials generally cool rapidly after laser treatment. To reduce the calculation time required for numerical simulation, the laser beam was fed through an S-shaped path (hereafter referred to as SSP), as illustrated in Fig. 3, which was employed in the heat treatment simulation model. Data were collected from nine nodes in the targeted treatment area (length: l_h ; width: 3 mm) on the surfaces of the steel materials, as shown in Fig. 4. In this article, the length of the proposed S-shaped laser track for the heat treatment was set at 3 mm to achieve a hardening width of 6 mm on the surface of the treatment area when the light spot diameter (R_i) was 3 mm.

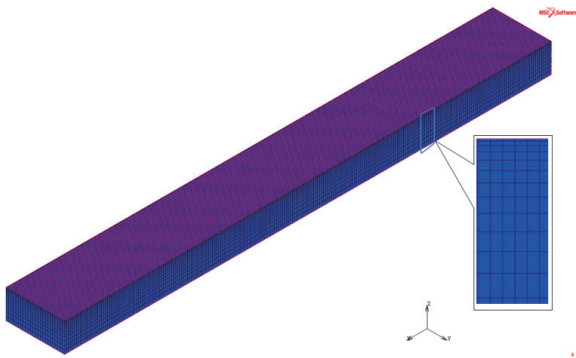


Fig. 1. (Color online) 3D finite element model mesh construction.

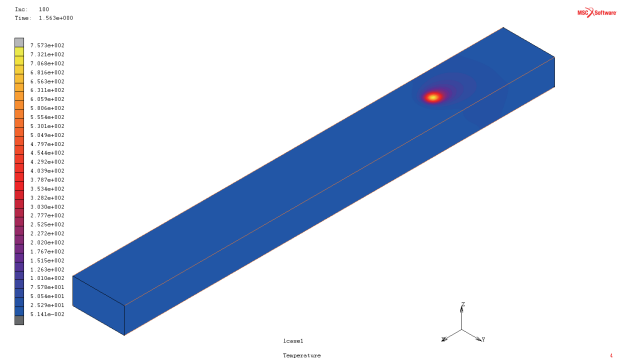


Fig. 2. (Color online) Moving heat source of laser.

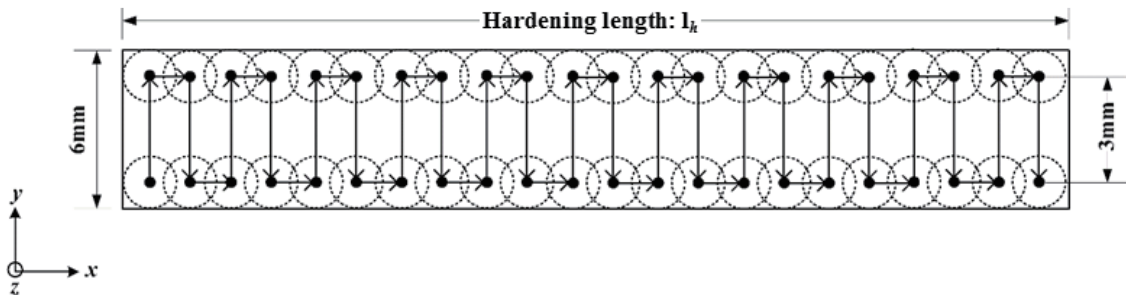


Fig. 3. SSP traced by multitrack laser heat treatment.

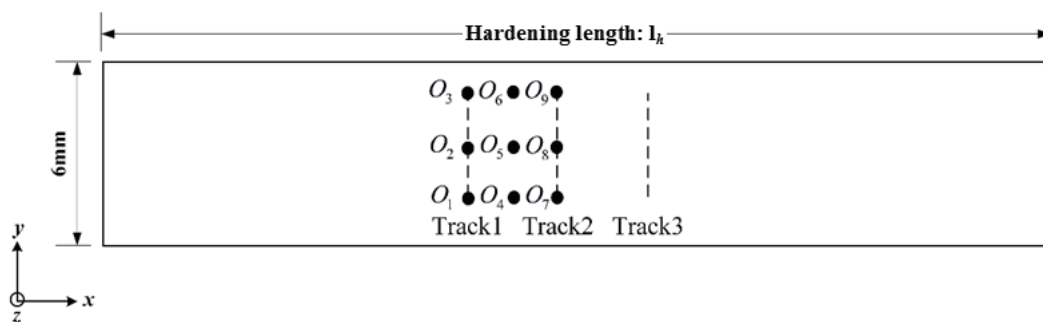


Fig. 4. Schematic of the nine nodes designating the data acquisition points during the multitrack laser heat treatment.

Figure 5 depicts the nine nodes (labeled O_1 – O_9) selected from the area between the first and second laser tracks for temperature data acquisition and further analysis. In terms of laser power output, laser power and energy were continuously fed from the beginning to the end of the SSP.

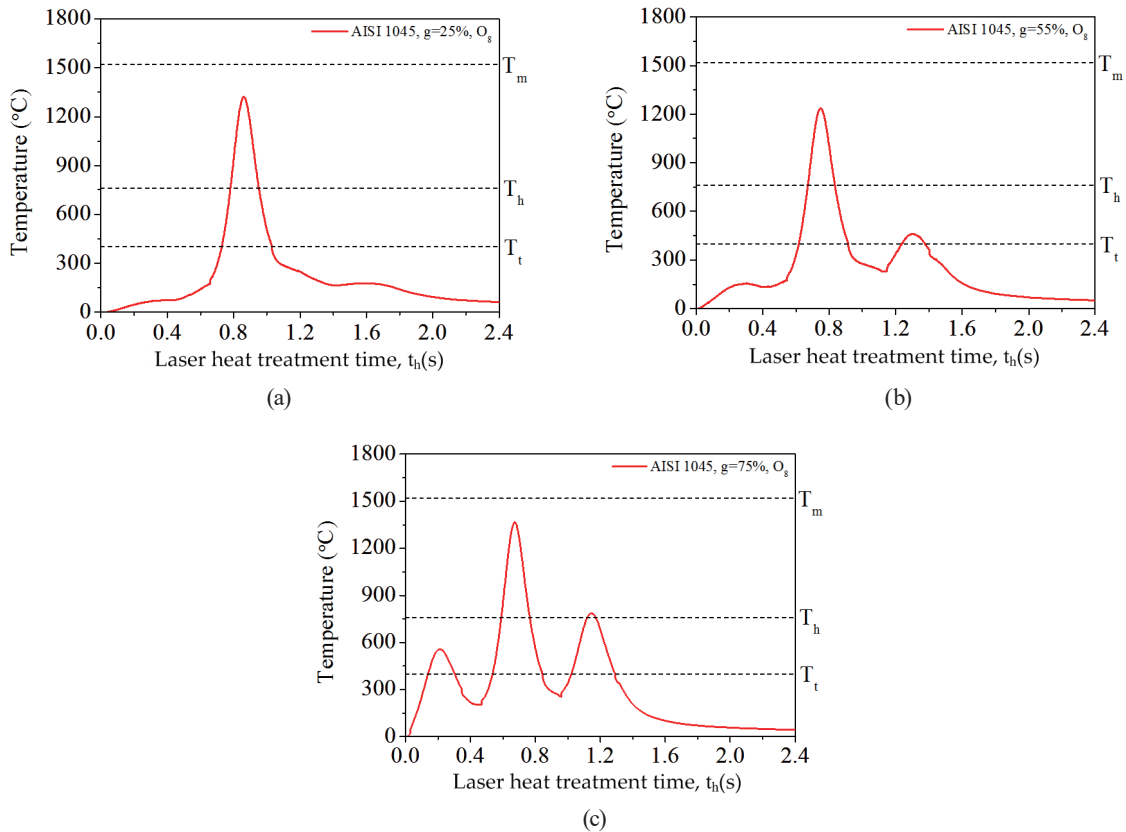


Fig. 5. (Color online) Temperature profiles of O_8 on AISI 1045 at laser overlap rates of (a) 25, (b) 55, and (c) 75%.

3. Results and Discussion

In this study, we examined the tempering effects of multitrack laser surface heat treatment by using the finite element method to simulate and analyze the effects of all process parameters on the heat treatment process. The appropriate ranges and optimal values of the process parameters were identified. The multitrack laser heat treatment process was analyzed to examine the tempering effects of these process parameters on multiple nodes along the surfaces of the materials. In the following subsection, the effects of laser overlap rate, laser power, laser feed rate, and laser spot size on the temperature distribution of AISI 1045 steel materials will be discussed. Because of the considerable amount of data collected from the nine nodes, not all of the nodes are presented in the figures; only nodes that reflected significant effects of the four parameters on temperature distribution, namely, O_8 and O_9 , are discussed. T_p denotes the highest peak temperature during the laser heat treatment.

3.1 Effects of laser overlap rate on tempering effects

This subsection focuses on analyzing the effects of laser overlap rate (g) on the temperature profiles of nodes O_8 and O_9 . The laser power P_i was set at 350 W, the laser feed rate V_i at 8 mm/s,

the laser spot size diameter R_i at 3 mm, and the laser feed path as the SSP. Figure 5 shows the temperature profiles of node O_8 (see Fig. 4) on the steel material for laser overlap rates of $g = 25$, 55, and 75%. It can be seen that these rates all generated temperatures above the quenching temperature T_h , which may have induced hardening. In addition, all of the O_8 temperatures reached the tempering temperature, which might have caused tempering effects. Note that the tempering effects of O_8 are relatively more prominent at $g = 75\%$. When the laser overlap rate is increased from 25 to 55%, the first peak temperature decreases by 7%, but the second peak temperature increases by 160%. When the overlap rate is increased from 55 to 75%, the first peak temperature increases by 252%, the second by 10%, and the third by 70%.

Figure 6 illustrates the temperature profiles of node O_9 on AISI 1045. Similarly to O_8 , the three laser overlap rates generated temperatures over the quenching temperature T_h and induced hardening. At $g = 55$ and 75%, tempering effects might have occurred on node O_9 , and these effects were more prominent. When the rate was increased from 25 to 55%, the first peak temperature remained unchanged, but the second peak temperature increased by 178%. When the rate increased from 55 to 75%, the first peak temperature increased by 14% and the second by 73%. From the information in Figs. 5 and 6, we selected the temperature profile of the 55% laser overlap rate to discuss the effects of laser power, laser feed rate, and laser spot size on the tempering effects of O_8 and O_9 .

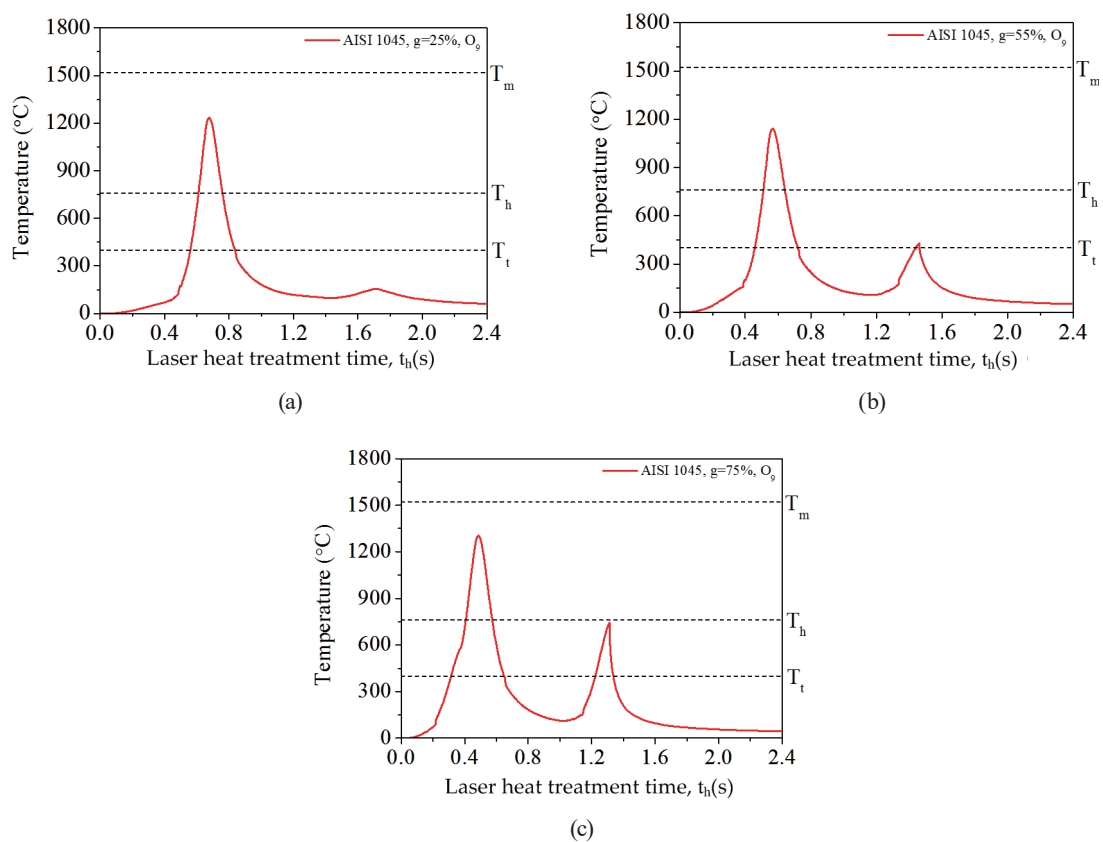


Fig. 6. (Color online) Temperature profiles of O_9 on AISI 1045 at laser overlap rates of (a) 25, (b) 55, and (c) 75%.

3.2 Effect of laser power on tempering effects

In this subsection, the effects of laser power on the temperature profiles of O₈ and O₉ are examined. The laser feed rate V_i was set at 8 mm/s, the laser spot size diameter R_i at 3 mm, the laser overlap rate g at 55%, and the laser feed path as the SSP. Figure 7 shows the temperature profiles of O₈ for laser powers of $P_i = 300, 350,$ and 400 W. All these powers generated heat over the quenching temperature T_h and may have induced hardening. When $P_i = 300$ W, the third peak temperature reached the tempering temperature T_t . However, when $P_i = 350$ and 400 W, the third peak temperature was higher than the tempering temperature T_t and might have caused tempering effects on the steel material. In particular, when $P_i = 400$ W, the temperature at node O₈ exceeded the melting temperature (T_m) of AISI 1045, which could cause the steel to melt.

Figure 8 presents the temperature profiles of O₉ for laser powers of $P_i = 300, 350,$ and 400 W. Similarly to O₈, the generated temperatures for these laser powers were higher than the quenching temperature T_h and hence might have caused hardening. However, the second peak temperature (tempering temperature) at node O₉ increased by around 15–17% when its laser power was increased by 50 W. We concluded that laser power control is not adaptive for SAE-AISI 1045 and that 350 W is the suitable laser power.

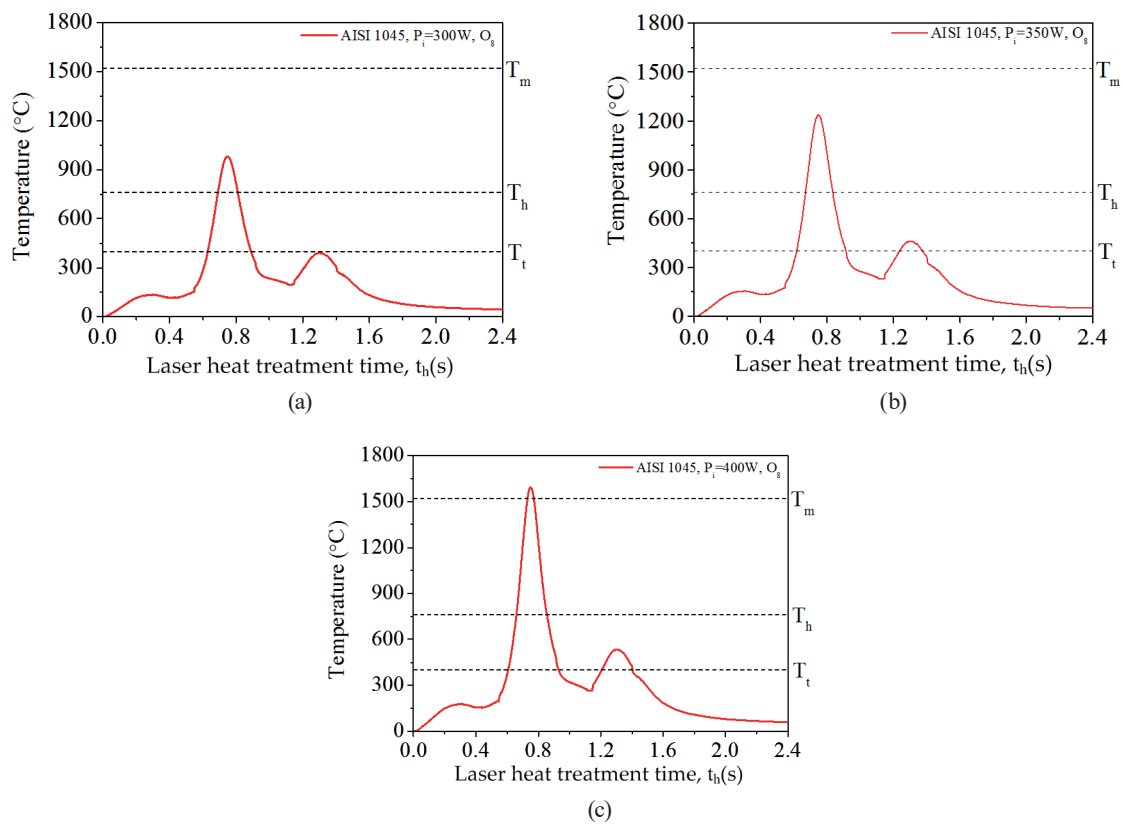


Fig. 7. (Color online) Temperature profiles of O₈ at laser powers of (a) 300, (b) 350, and (c) 400 W.

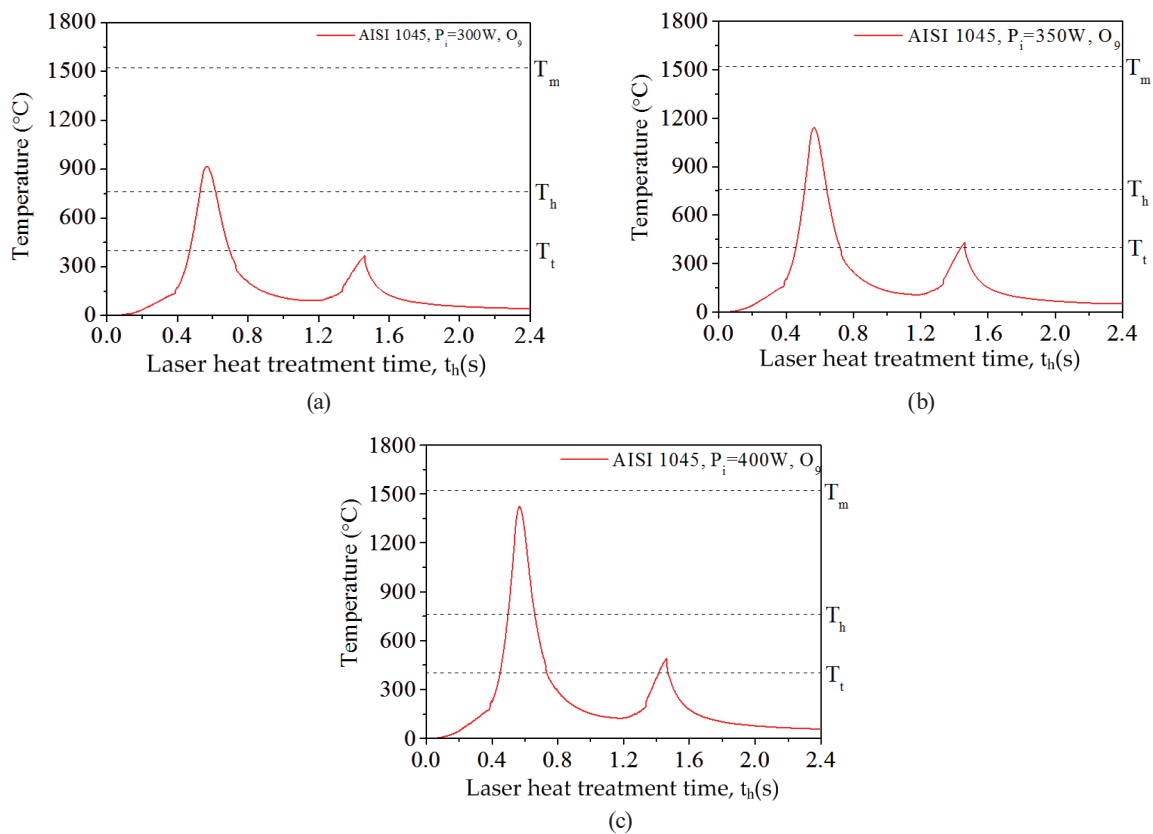


Fig. 8. (Color online) Temperature profiles of O_9 at laser powers of (a) 300, (b) 350, and (c) 400 W.

3.3 Effect of laser feed rate on tempering effects

In this subsection, the effects of laser feed rate on the temperature profiles of O_8 and O_9 are explored. The laser power P_l was set at 350 W, the laser spot size diameter R_l at 3 mm, the laser overlap rate g at 55%, and the laser feed path as the SSP. The temperature profiles of node O_8 are given in Fig. 9 for three laser feed rates of $V_f = 5, 10,$ and 15 mm/s. The temperatures on node O_8 are higher than T_h and could result in hardening. In these cases, the second peak temperature exceeded the tempering temperature T_t , causing tempering effects. Figure 10 presents the temperature profiles of node O_9 for AISI 1045 at three different laser feed rates. These rates also contributed to heated temperatures higher than T_h on O_9 that might cause hardening. For laser feed rates of 5 and 10 mm/s, the second peak temperature reached or exceeded the tempering temperature T_t and therefore would also cause tempering effects. A laser feed rate of 15 mm/s would not induce tempering effects because the second peak temperature did not exceed T_t . Note that the second peak temperature (tempering temperature) of node O_9 for AISI 1045 was reduced by approximately 13–18% when the laser feed rate was increased by 5 mm/s. From the simulation results shown in Figs. 9 and 10, we can conclude that tempering effects are better at node O_9 than at node O_8 .

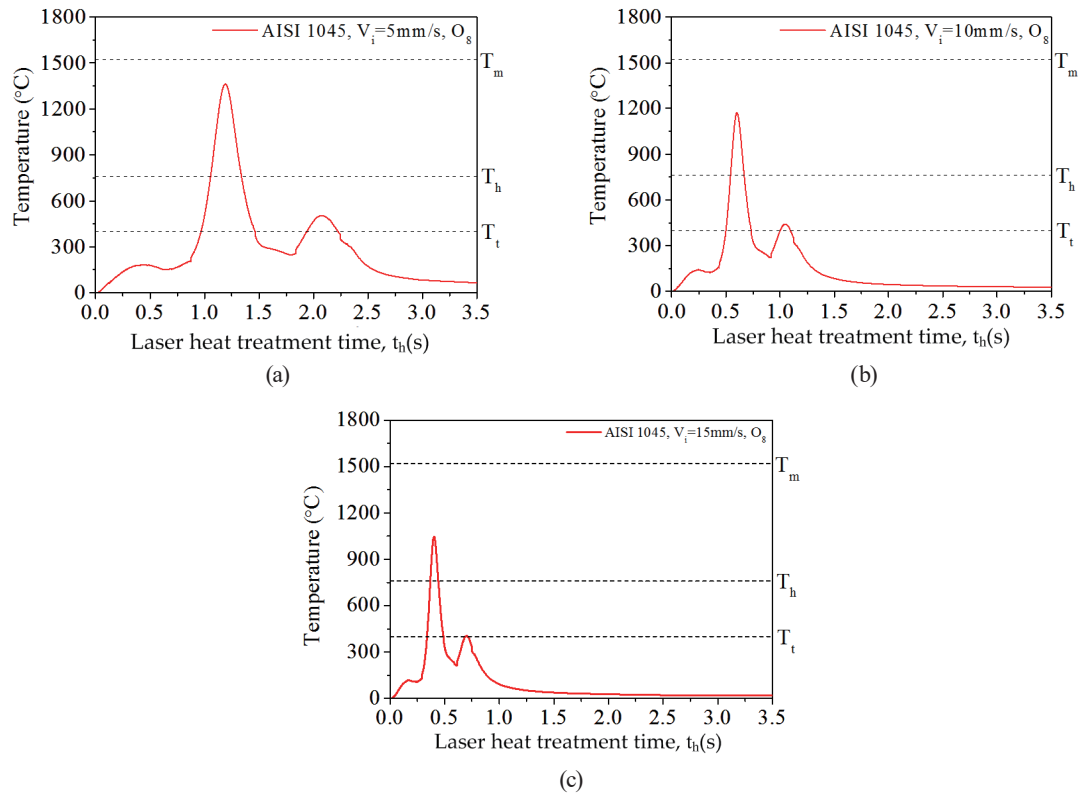


Fig. 9. (Color online) Temperature profiles of O_8 at laser feed rates of (a) 5, (b) 10, and (c) 15 mm/s.

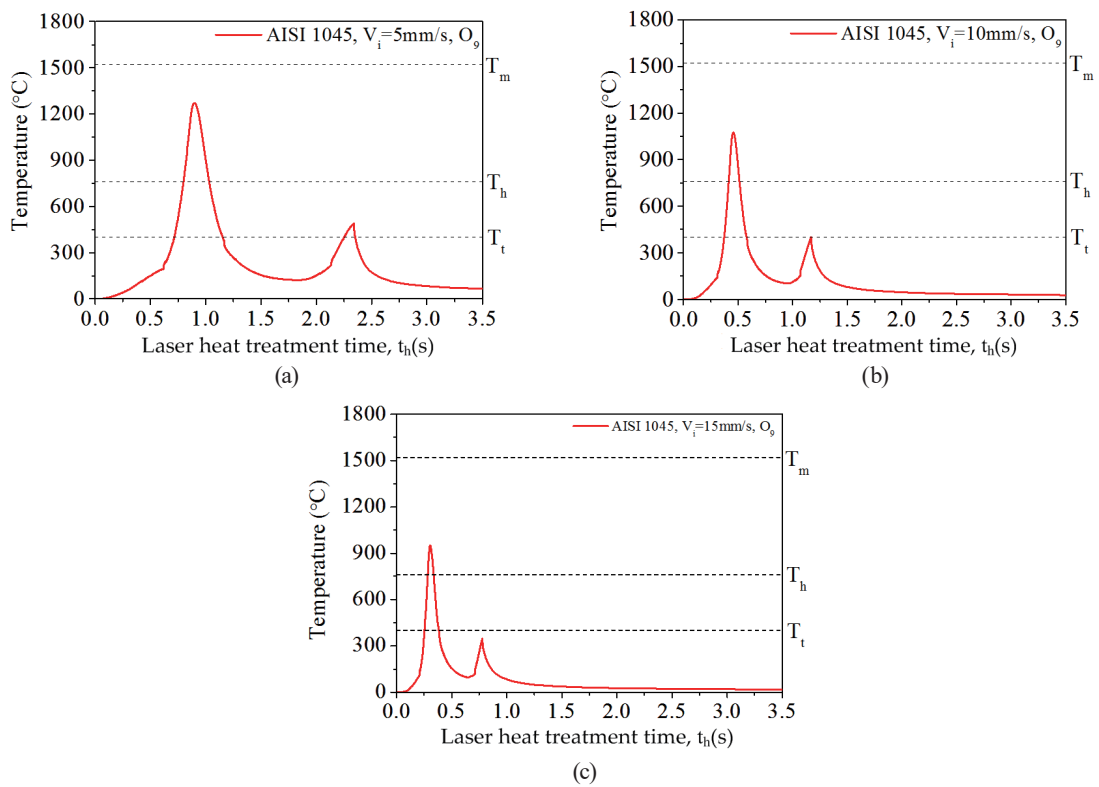


Fig. 10. (Color online) Temperature profiles of O_9 at laser feed rates of (a) 5, (b) 10, and (c) 15 mm/s.

3.4 Effect of laser spot size on tempering effects

In this subsection, the effects of laser spot size on the temperature profiles of O_8 and O_9 are analyzed. The laser power P_i was set at 350 W, the laser feed rate V_i at 8 mm/s, the laser overlap rate g at 55%, and the laser feed path as the SSP. Figures 11 and 12 respectively depict the temperature profiles of O_8 and O_9 for laser spot diameters of $R_i = 2.8, 3.0,$ and 3.2 mm. It can be observed from Figs. 11 and 12 that these spot diameters produced a temperature higher than T_h at both O_8 and O_9 , inducing hardening. Note that AISI 1045 could also melt when $R_i = 2.8$ mm because the heated temperature exceeded its melting temperature T_m . Also, note that the tempering effects of O_8 and O_9 would only occur when $R_i = 3$ mm.

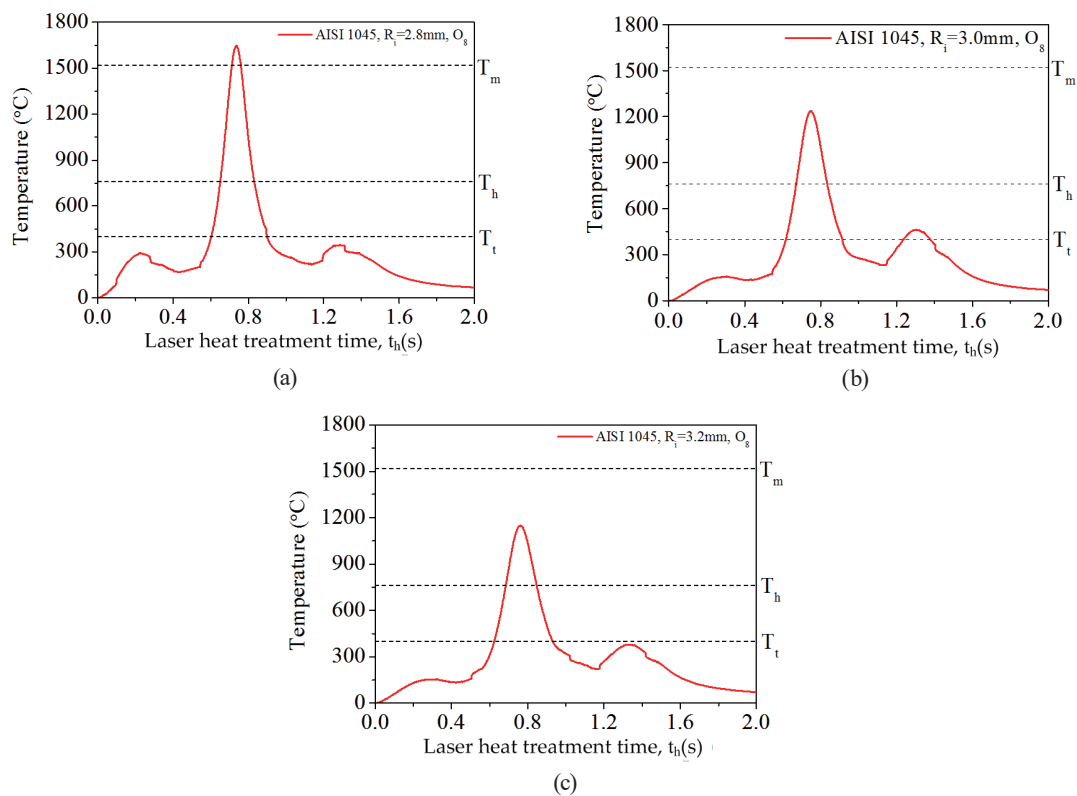


Fig. 11. (Color online) Temperature profiles of O_8 at spot sizes of $R_i =$ (a) 2.8, (b) 3, and (c) 3.2 mm.

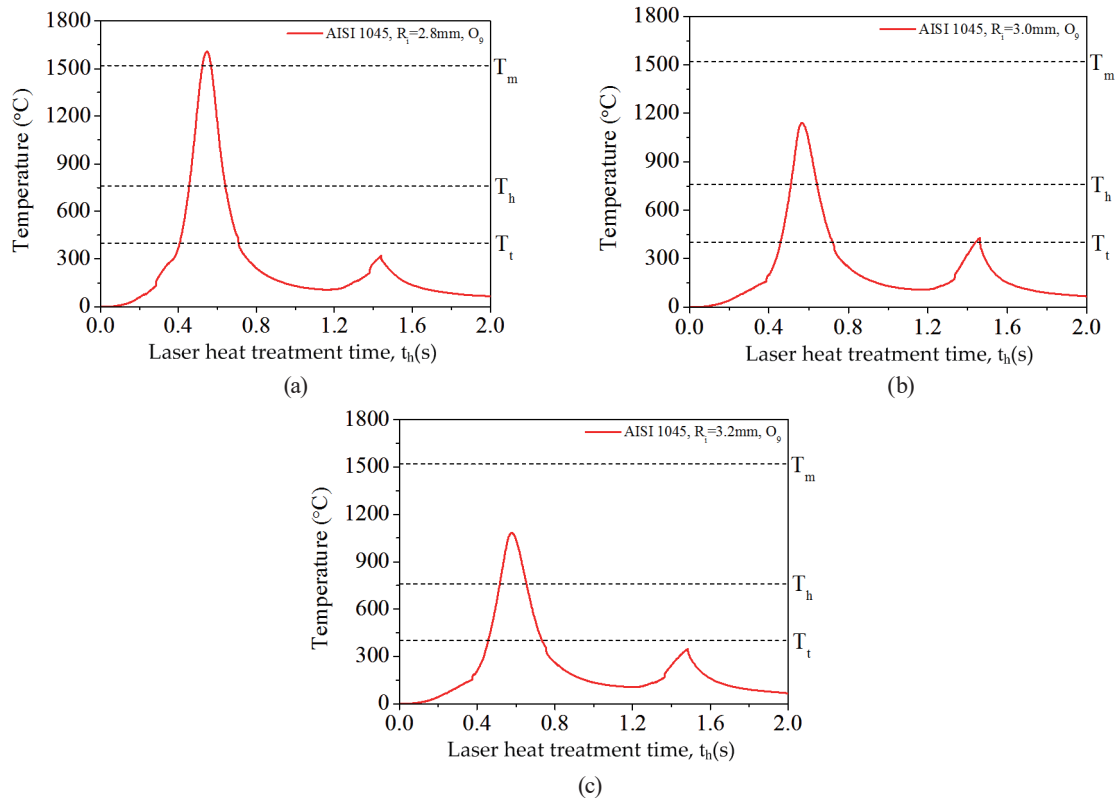


Fig. 12. (Color online) Temperature profiles of O_9 at spot sizes of $R_i =$ (a) 2.8, (b) 3, and (c) 3.2 mm.

4. Conclusions

In this study, a thermal–mechanical coupling model was utilized to simulate the peak temperature at the center of a laser spot as well as the hardening width and depth for various laser process parameters during the multitrack heat treatment of AISI 1045 medium carbon steel using a Nd:YAG laser. A finite element analysis model was proposed to effectively analyze the temperature field distribution on the surface of AISI 1045 for various process parameters during laser heat treatment. The obtained temperature field distributions on the material surface were used to observe and estimate the uniformity of the hardened surface layer and the relationship between tempering effects and process parameters. The appropriate ranges of the four process parameters—laser power, laser spot size, laser feed rate, and laser overlap rate—were identified for multitrack laser heat treatment. Numerical results reveal that the proposed finite element models are feasible for simulating the laser surface heat treatment process and tempering effects on AISI 1045 steel. Hence, the results may serve as a useful reference for researchers regarding the process parameters of laser heat treatment when conducting machining experiments.

Acknowledgments

The authors acknowledge partial financial support under grant no. MOST 106-2221-E-151-017.

References

- 1 J. H. Gur and J. Pan: Handbook of Thermal Process Modeling Steels (CRC Press, Boca Raton, 2009) p. 499.
- 2 T. Maiman: Phys. Rev. Lett. **4** (1960) 564. <https://doi.org/10.1103/PhysRevLett.4.564>
- 3 T. Maiman: Nature **187** (1960) 493. <https://doi.org/10.1038/187493a0>
- 4 C. DeMichelis: IEEE J. Quantum Electron. **QE-6** (1970) 630. <https://doi.org/10.1109/JQE.1970.1076329>
- 5 D. Lichtman and J. F. Ready: Phys. Rev. Lett. **10** (1963) 342. <https://doi.org/10.1103/PhysRevLett.10.342>
- 6 G. R. Speich and A. Szirmai: Transform. Metall. Soc. AIME **245** (1969) 1063.
- 7 S. Namba, P. H. Kim, S. Nakayama, and I. Ida: Jpn. J. Appl. Phys. **4** (1965) 153. <https://doi.org/10.1143/JJAP.4.153>
- 8 D. Belforte and M. Levitt: Industrial Laser Handbook (Springer-Verlag, New York, 1992) p. 13.
- 9 C. Wick: Manuf. Eng. **76** (1976) 35.
- 10 J. E. Miller and J. A. Wineman: Metal Prog. **111** (1977) 38.
- 11 J. R. Loeffler: Assembly Eng. **20** (1977) 32.
- 12 P. W. Fuerschbach and D. O. MacCallum: Proc. 14th Int. Congress on Applications of Lasers & Electro-Optics (1995) 493–497.
- 13 M. Bojinović, N. Mole, and B. Štok: Surf. Coat. Technol. **273** (2015) 60. <https://doi.org/10.1016/j.surfcoat.2015.01.075>
- 14 Q. Nguyen and C.-Y. Yang: Int. J. Heat Mass Transfer **95** (2016) 224. <https://doi.org/10.1016/j.ijheatmasstransfer.2015.11.087>
- 15 S. Sarkar, M. Gopinath, S. S. Chakraborty, B. Syed, and A. K. Nath: Surf. Coat. Technol. **302** (2016) 344. <https://doi.org/10.1016/j.surfcoat.2016.06.045>
- 16 S. Martínez, A. Lamikiz, E. Ukar, A. Calleja, J. A. Arrizubieta, and L. N. Lopez de Lacalle: Opt. Lasers Eng. **90** (2017) 72. <https://doi.org/10.1016/j.optlaseng.2016.10.005>
- 17 R. S. Lakhkar, Y. C. Shin, and M. J. M. Krane: Mater. Sci. Eng., A **480** (2008) 209. <https://doi.org/10.1016/j.msea.2007.07.054>
- 18 F. Cordovilla, Á. García-Beltrán, P. Sancho, J. Domínguez, L. Ruiz-de-Lara, and J. Ocaña: Mater. Design **102** (2016) 225. <https://doi.org/10.1016/j.matdes.2016.04.038>
- 19 K. Wissenbach, A. Gillner, F. Dausinger, E. Beyer, and K. Wissenbach: Oberflächenbehandlung mit Laserstrahlung. Allgemeine Grundlagen (Springer-Verlag, Berlin, 1998) p. 19 (in German).
- 20 H. T. Ding and S. Yung: J. Manuf. Sci. Eng. **10** (2012) 051014. <https://doi.org/10.1115/1.4007464>
- 21 T. Kusuhara, J. Morimoto, N. Abe, and M. Tsukamoto: Proc. 4th Int. Conf. Modeling, Simulation and Applied Optimization (IEEE, 2011) 1–4.
- 22 C. Dawes: Laser Welding (Ablington Publishing and Woodhead Publishing in Association with the Welding Institute, Cambridge, 1992) p. 1.
- 23 T. Zacharia, S. A. David, J. M. Vitek, and T. Debroy: Weld. J. **68** (1989) 499.
- 24 T. Zacharia, S. A. David, J. M. Vitek, and T. Debroy: Weld. J. **68** (1989) 510.
- 25 J. DeKock: Laser Heat Treating Advances for the Gear Industry. <http://www.gearsolutions.com/article/detail/5632/laser-heat-treating-advances-for-the-gear-industry> (accessed 2 April 2018).